A ROBUST SUPER TWISTING CONTROL FOR A DOUBLY-FED INDUCTION GENERATOR SUPPLIED BY A NINE-SWITCH CONVERTER

Younes DRIS[1], Mohamed Choukri BENHABIB[2], Sidi Mohammed MELIANI[3], Virgil DUMBRAVA[4]

This article presents an efficient control scheme for a wind turbine based on a doubly fed induction generator. The nine-switch converter (NSC) is used to connect the rotor windings to the grid. This proposed converter is controlled by the super twisting control (STC) to extract the maximum power from the wind turbine, to keep the DC bus voltage constant and to eliminate harmonic currents. A comparison was made to demonstrate the high robustness of the STC. The studied system is simulated using MATLAB SimPowerSystem. The results show the ability of the NSC to remove harmonic currents where the power quality has improved significantly. The reliability of the STC is proven in terms of tracking and robustness.

Keywords: Wind turbine; Doubly fed induction generator DFIG; Nine switch converter NSC; Super twisting control; Harmonic currents; Power quality; SimPowerSystem

1. Introduction

Nowadays, the great challenge is to produce clean and safe energy at a lower cost. For that, researchers are developing renewable energy as an alternative to conventional energy. Among these recent electricity generation technologies, wind energy is the most promising [1]. The worldwide cumulative installed wind power capacity has grown exponentially to reach 651 GW by the end of 2019 [2]. Many wind energy conversion systems (WECS) have been developed but the doubly-fed induction generator (DFIG) is the most attractive because of the small rate of converters and the flexible power control [3]. The stator of DFIG is connected directly to the grid and the rotor windings are linked to the grid by a

[1] Laboratoire d'automatique (LAT), Université de Tlemcen, Algeria, e-mail: younes.dris@univ-tlemcen.dz

[2] Manufaturing Engineering Laboratory (MELT), Université de Tlemcen, Algeria, e-mail: mohamedchoukri.benhabib@univ-tlemcen.dz

[3] Manufaturing Engineering Laboratory (MELT), Université de Tlemcen, Algeria, e-mail: sidimohammed.meliani@univ-tlemcen.dz

[4] Faculty of Power Engineering, University POLITEHNICA of Bucharest, Romania, e-mail: v_dumbrava@yahoo.com

converter. Several converter topologies dedicated to wind energy conversion are presented and discussed according to their advantages/disadvantages in [4]. The conventional two-level back-to-back voltage source converter used in [5] is the most popular wind power converter. In [6], the same topology is used with a parallel configuration, it designed for high current systems. In [7], the multilevel converter is used, which has the ability to deal with larger power capacities. However, this topology also has some disadvantages, such as the high number of semiconductor devices. For this, researchers have developed other converters such as the five-leg converter used in [8]. This converter uses less power electronics, but its control is more complicated. In [9], the nine-switch converter (NSC) is used as an active filter and in [10], it is employed in the DFIG for the first time. This last converter is very attractive because it has fewer semiconductor components and its control is very simple. In [11], they have used the conventional control based on the proportional-integral regulator (PI) but the robustness of this system has not been tested. In [12], the predictive control is used and the result shows the effectiveness of the control, but it is more complicated. In [13], the direct torque control (DTC) is employed and in [14], the sliding mode control (SMC) is carried out experimentally. The chattering introduced by the DTC and the SMC has made them unfavorable in many applications. In grid connection applications, the quality of the power produced can be degraded by the high chattering or by the presence of the non-linear load. To solve this problem, we propose in our paper to use the super twisting control (STC) to achieve high robustness with less chattering and introduce the filtering ability of the nine-switch converter to eliminate the harmonic currents.

2. System description

The system under study consists of three parts. The first part is the mechanical part which is responsible for capturing the energy of the wind and it is made up of blades and the gearbox. The second part is the electrical part which consists of the DFIG which produces power at constant voltage and constant frequency though the rotor speed varies. The windings of the stator are connected directly to the grid while the rotor windings are connected to the grid through the NSC. The third part is the control part which is the most important element in this study. The decoupled d-q vector control technique is used with the non-linear control STC to achieve high robustness and to ensure high quality of energy. The aim of this control is to extract the maximum power from the turbine, control the power exchanged between the grid and the DFIG and keep the DC bus voltage constant at the desired value. Fig. 1 shows the configuration of the DFIG system connected to the 690V/50Hz grid utility. A nonlinear load is used to inject harmonics current which consists of a rectifier (6 diodes) and an RL load.

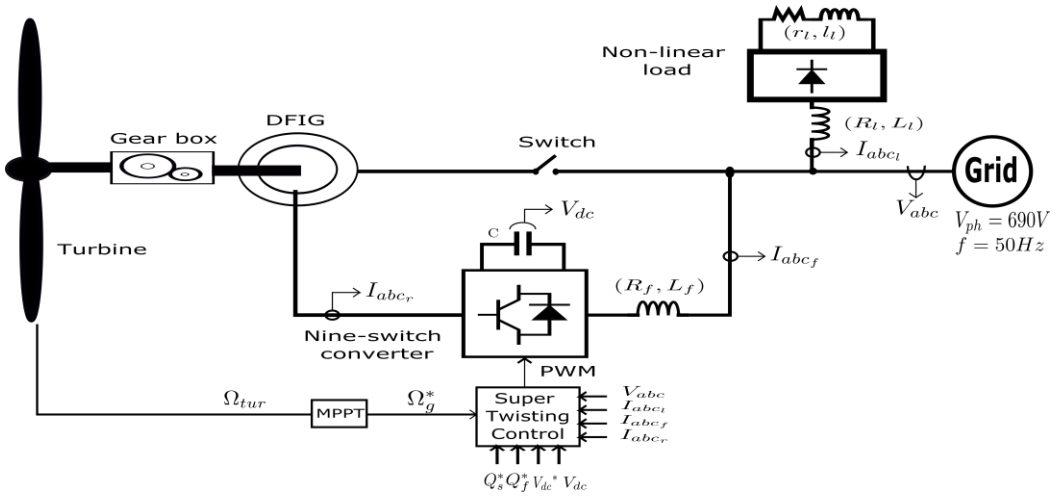

Fig. 1. Doubly fed induction generator feed by the NSC topology.

In this work, the power of the load is less than the power produced by the DFIG. The remaining power produced by the DFIG is delivered to the grid.

2.1. Mechanical part modelling of the wind turbine

The relation between the wind speed and the power captured is described by the following equation:

$$P_t = \frac{1}{2}\rho\pi R^2 V_v^3 C_p(\lambda,\beta) \tag{1}$$

where P_t is the power captured by the wind turbine, ρ is the air density, V_v is the wind speed, R is the length of the blades (radius of the turbine rotor), and $C_p(\lambda,\beta)$ is the power coefficient which depends on both the tip speed ratio λ and the blade pitch angle β.

The model of the drive train is given by the following equation:

$$\begin{cases} J\dfrac{d\Omega_g}{dt} = \dfrac{C_{tur}}{G} - C_{em} \\ J = \dfrac{J_{tur}}{G^2} + J_g \end{cases} \tag{2}$$

where J_{tur} and J_g are the inertia of the turbine and the DFIG respectively. C_{tur} and C_{em} are the turbine torque and the electromagnetic torque respectively. Ω_g is the speed of the DFIG. G is the gearbox ratio.

2.2. Electrical part modelling of the wind turbine

2.2.1. Dynamic model of the DFIG

The DFIG is an asynchronous generator. The most important feature of the DFIG is that it is connected on both the stator side and the rotor side, where the stator is directly connected to the grid, and the rotor is interfaced via the NSC. The stator and rotor voltages in the synchronous farm are presented as follows:

$$\begin{cases} V_{sd} = R_s I_{sd} + \dfrac{d\varphi_{sd}}{dt} - \omega_s \varphi_{sq} \\ V_{sq} = R_s I_{sq} + \dfrac{d\varphi_{sq}}{dt} + \omega_s \varphi_{sd} \\ V_{rd} = R_r I_{rd} + \dfrac{d\varphi_{rd}}{dt} - \omega_r \varphi_{rq} \\ V_{rq} = R_r I_{rq} + \dfrac{d\varphi_{rq}}{dt} + \omega_r \varphi_{rd} \end{cases} \tag{3}$$

where I_{sd}, I_{sq}, I_{rd} and I_{rq} are the stator and rotor currents respectively. R_s and R_r are the stator and rotor resistances respectively. ω_s and ω_r are the angular frequency of the stator and the rotor components respectively. φ_{sd}, φ_{sq}, φ_{rd} and φ_{rq} are the magnetic flux of the stator and the rotor respectively.

2.2.2. Dynamic model of the RL filter and the DC bus voltage:

The mathematical model of the filter and the continuous bus can be expressed as follows:

$$\begin{cases} V_{fd} = -R_f I_{fd} - L_f \dfrac{dI_{fd}}{dt} + \omega_s L_f I_{fq} + V_{sd} \\ V_{fq} = -R_f I_{fq} - L_f \dfrac{dI_{fq}}{dt} - \omega_s L_f I_{fd} + V_{sq} \\ \dfrac{dV_{dc}}{dt} = \dfrac{1}{C} I_c \end{cases} \tag{4}$$

where V_{fd}, V_{fq} and V_{dc} are the voltages of the filter and the DC bus respectively. I_{fd}, I_{fq} are the currents of the RL filter. I_c is the current of the capacitor C. R_f and L_f are the resistances and the inductance of the RL filter.

2.2.3. Nine switch converter topology:

The nine-switch converter (NSC) has only three legs on which three switches are installed. This converter is like two inverters had common switches. The top three switches and the middle three switches are equivalent to the grid

side converter (GSC) and the bottom three switches and the middle three switches represent the rotor side converter (RSC). The DC bus voltage is connected to the upper and lower rail of the NSC. Fig. 2 shows the diagram of the NSC.

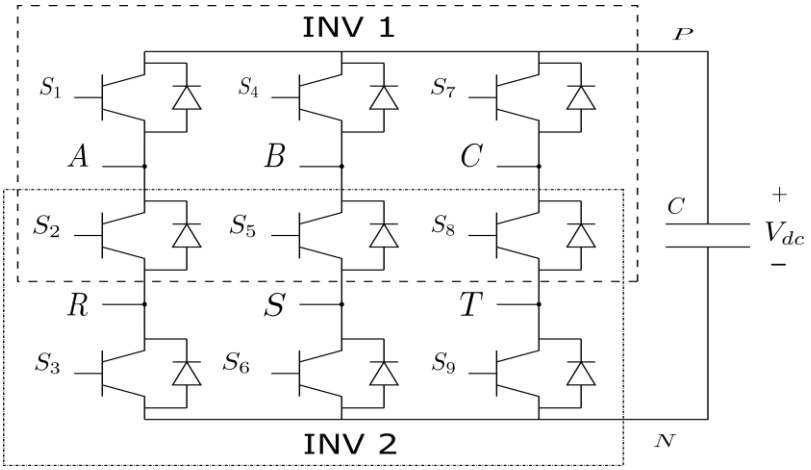

Fig. 2. Diagram of the nine-switch converter NSC.

The NSC has two modes of operation: the constant frequency mode and the variable frequency mode. In this paper, the variable frequency mode was chosen because the DFIG system requires that the magnitude and frequency of the RSC must be adjustable. Due to the reduced number of switches in the NSC, there are only three switching states per phase. Table 1 shows the switching pattern design of the NSC [15].

Table 1

Switching states and converter leg voltages

Switching state	S_1	S_2	S_3	V_{AN}	V_{RN}
1	ON	ON	OFF	V_{dc}	V_{dc}
2	OFF	ON	ON	0	0
3	ON	OFF	ON	V_{dc}	0

It is obvious that the voltage V_{RN} must not exceed the voltage V_{AN}. Thus, the modulation function is designed as follows:

$$\begin{cases} S_1 + S_2 + S_3 = 2 \\ V_{AN} \geq V_{RN} \end{cases} \tag{5}$$

As mentioned above, the variable frequency mode is used. For this, the sum of the two modulation indices m_1 and m_2 of INV 1 and INV 2 must not exceed 1. To comply with the switching constraint, a DC offset of 0.5 and -0.5 is added to the input modulating signals m_1 and m_2 respectively. The modified modulation index is given as follows:

$$\begin{cases} m_1 = \dfrac{2V_{f_{abc}}}{V_{dc}} + \dfrac{1}{2} \\ m_1 = \dfrac{2V_{r_{abc}}}{V_{dc}} - \dfrac{1}{2} \end{cases} \tag{6}$$

where $V_{f_{abc}}$ and $V_{r_{abc}}$ are the voltage reference of the GSC and the RSC respectively. Both modulating waves m_1 and m_2 are compared with a common triangle wave, and each is adjusted to half of the carriers magnitude. Therefore, the DC bus voltage V_{dc} of the NSC is twice as high as the rated DC bus voltage of the conventional back-to-back converter with the same AC ratings. Fig. 3 shows the diagram of the gate signal generation using logic gates.

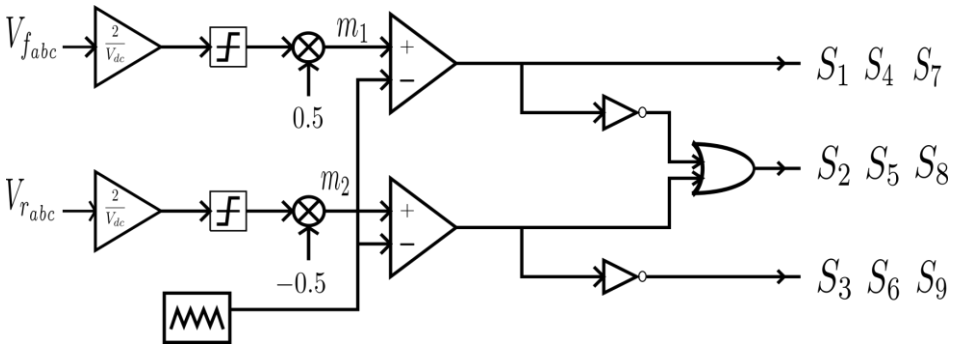

Fig. 3. Diagram of the gate signal generation using logic gates.

2.3. Control of the DFIG

The control of the DFIG consists of two parts. The first one is the RSC control, which is responsible for extracting the maximum power and controlling the power exchanged between the stator of the DFIG and the grid. The second part is the GSC control, which is responsible for keeping the DC bus voltage constant and eliminating harmonic currents. In this study, the STC is used to achieve high robustness with low chattering. The global control law of the STC is composed of two terms, the equivalent term V_{equ} and the STC term U_{st} [16].

$$U = V_{equ} + U_{st} \tag{7}$$

The first term can be obtained by solving the equation below:

$$\dot{S} = 0 \tag{8}$$

where S is the sliding surface. The second term is the super twisting control which is given as follows:

$$\begin{cases} U_{st} = V_1 + V_2 \\ V_1 = -K_1 \left|S\right|^r Sign(S) \\ \dot{V}_2 = -K_2 Sign(S) \end{cases} \tag{9}$$

where K_1, K_2 are chosen through a random tuning to achieve the convergence of the control laws and r is defined as 0 < r < 1 [17]. The choice of r = 0.5 assures that the sliding order 2 is well achieved [18].

2.3.1. RSC control

By applying vector control, the stator flux is oriented along the d-axis $(\varphi_{sq} = 0)$. The active power, reactive power and the electromagnetic torque are expressed as follows:

$$\begin{cases} P_s = \dfrac{3}{2} V_{sq} I_{sq} \\ Q_s = \dfrac{3}{2} V_{sq} I_{fd} \\ C_{em} = \dfrac{-3pM\varphi_{sd}}{2L_s} I_{rq} \end{cases} \tag{10}$$

where p is the is the number of pole pairs. L_s is the stator inductance. M is the mutual inductance. The cascade control is used in this article, where the outer loop is responsible for extracting the maximum power and the inner loop is used to control the power exchanged between the grid and the stator.

- Maximum power point tracking (MPPT) control:

To extract the maximum power from the wind turbine, the MPPT control is needed to track the optimal speed. The sliding surface is chosen as follows:

$$S_{\Omega_g} = \Omega_g^* - \Omega_g \tag{11}$$

The equivalent control is given by the following equation:

$$C_{em_{equ}} = -\frac{1}{J}\dot{\Omega}_g^* + \frac{1}{G} C_{tur} \tag{12}$$

Fig. 4 shows the diagram of the MPPT control.

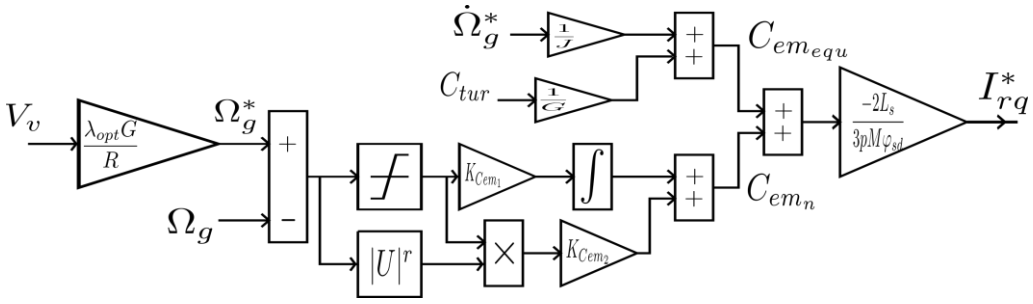

Fig. 4. Diagram of the MPPT control.

- Control of the rotor currents:

The sliding surfaces are chosen as follows:

$$\begin{cases} S_{I_{rd}} = I_{rd}^* - I_{rd} \\ S_{I_{rq}} = I_{rq}^* - I_{rq} \end{cases} \tag{13}$$

Applying the vector control and neglecting the stator resistance, the equivalent control is given by the following equation:

$$\begin{cases} V_{rd_{equ}} = R_r I_{rd} - \sigma L_r \omega_r I_{rq} + \sigma L_r \dot{I}_{rd}^* \\ V_{rq_{equ}} = R_r I_{rq} + \sigma L_r \omega_r I_{rd} + \sigma L_r \dot{I}_{rq}^* - \dfrac{\omega_r V_{sq} M}{\omega_s L_s} \end{cases} \tag{14}$$

where σ is the machine leakage coefficient. L_r is the rotor inductance.
Fig. 5 shows the diagram of the rotor current control.

2.3.2. GSC control

This control is performed through two loops, the outer loop is designed to control the DC bus voltage and the inner loop is used to control both active and reactive power. By applying the voltage vector control, the expression of the power will be expressed as follows:

$$\begin{cases} P_f = \dfrac{3}{2} V_{sq} I_{fq} \\ Q_f = \dfrac{3}{2} V_{sq} I_{fd} \end{cases} \tag{15}$$

- Control of the DC bus voltage:

This loop is used to keep the DC bus voltage constant. The sliding surface is chosen as follows:

$$S_{V_{dc}} = V_{dc}^{*} - V_{dc} \tag{16}$$

The equivalent control is given by the following equation:

$$I_{c_{equ}} = C\dot{V}_{dc}^{*} \tag{17}$$

Applying the vector control and neglecting the losses in the converter, the filter current will be described as follows [19]:

$$I_{fq} = \frac{2\left(V_{dc}I_{c} - P_{r}\right)}{3V_{qs}} \tag{18}$$

where P_r is the power of the rotor. Fig. 6 shows the diagram of the DC bus voltage.

- Control of the filter currents:

The presence of the non-linear load produces harmonic currents, so the filter current in the frame d - q can be expressed as follows [20]:

$$\begin{cases} I_{fd} = \bar{I}_{fd} + \tilde{I}_{fd} \\ I_{fq} = \bar{I}_{fq} + \tilde{I}_{fq} \end{cases} \tag{19}$$

where – and ~ denote both continuous and harmonic components. For compensating the reactive power, the d component of the current is reversed and used as a reference.

While eliminating the harmonic currents, they must first be extracted from the fundamental current. For that, we have used a high pass filter. The filter transfer function is given as follows:

$$H_{SOF} = \frac{s^{2}}{s^{2} + 2\zeta\omega_{n}s + \omega_{n}^{2}} \tag{20}$$

where: ζ is the damping ratio and ω_n is the natural frequency. Fig. 7 shows the block diagram of the high pass filter. In this paper, we consider that the output of the DC bus voltage control is the continuous component and we add the harmonic component extracted from the filter to construct the reference current of the internal loop.

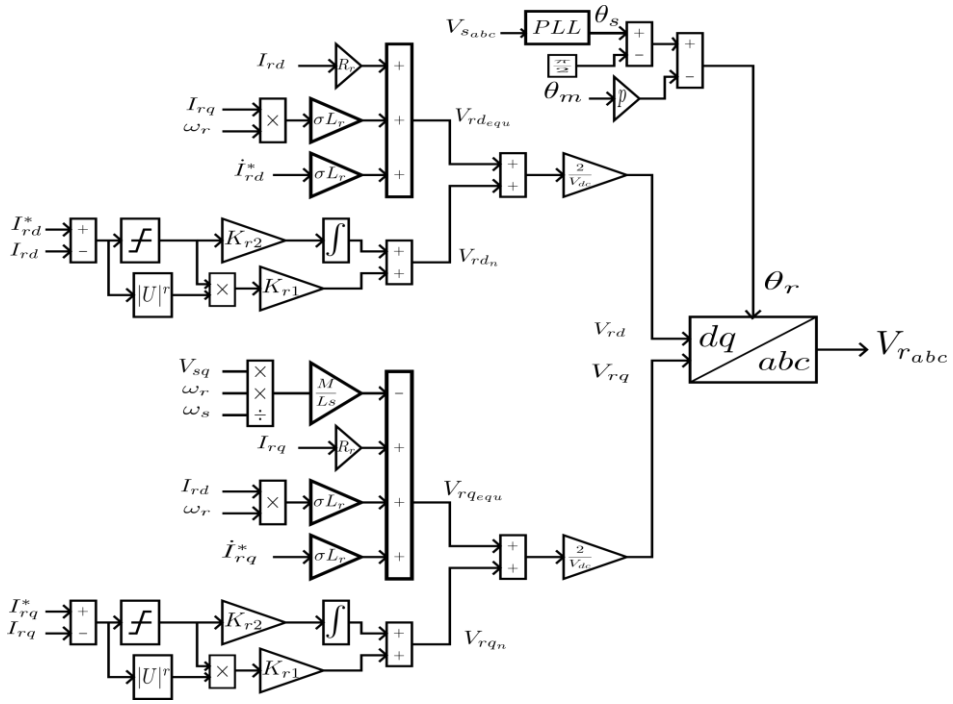

Fig. 5. Diagram of the rotor current control.

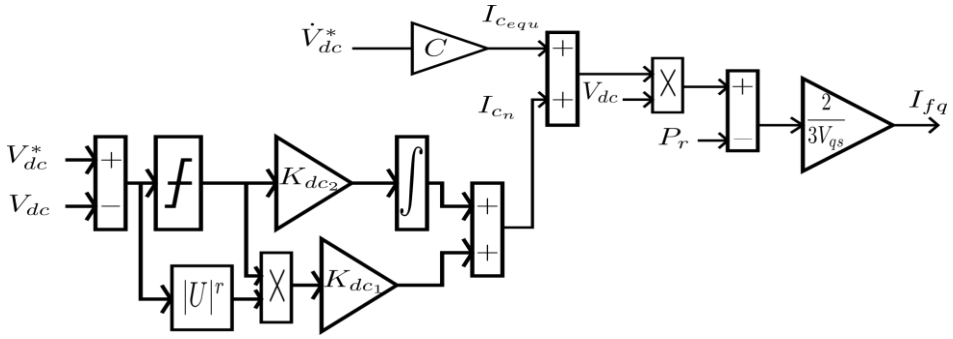

Fig. 6. Diagram of the DC bus voltage.

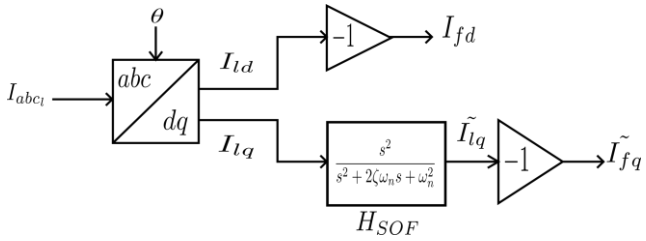

Fig. 7. Diagram of the high pass filter.

The sliding surfaces are chosen as follows:

$$\begin{cases} S_{I_{fd}} = I_{fd}^{*} - I_{fd} \\ S_{I_{fq}} = I_{fq}^{*} - I_{fq} \end{cases} \tag{21}$$

The equivalent control is given by the following equation:

$$\begin{cases} V_{fd_{equ}} = -R_f I_{fd} + L_f \omega_s I_{fq} - L_f \dot{I}_{fd}^{*} \\ V_{fq_{equ}} = -R_f I_{fq} - L_f \omega_s I_{fd} - L_f \dot{I}_{fq}^{*} + V_{sq} \end{cases} \tag{22}$$

Fig. 8 shows the diagram of the filter current control.

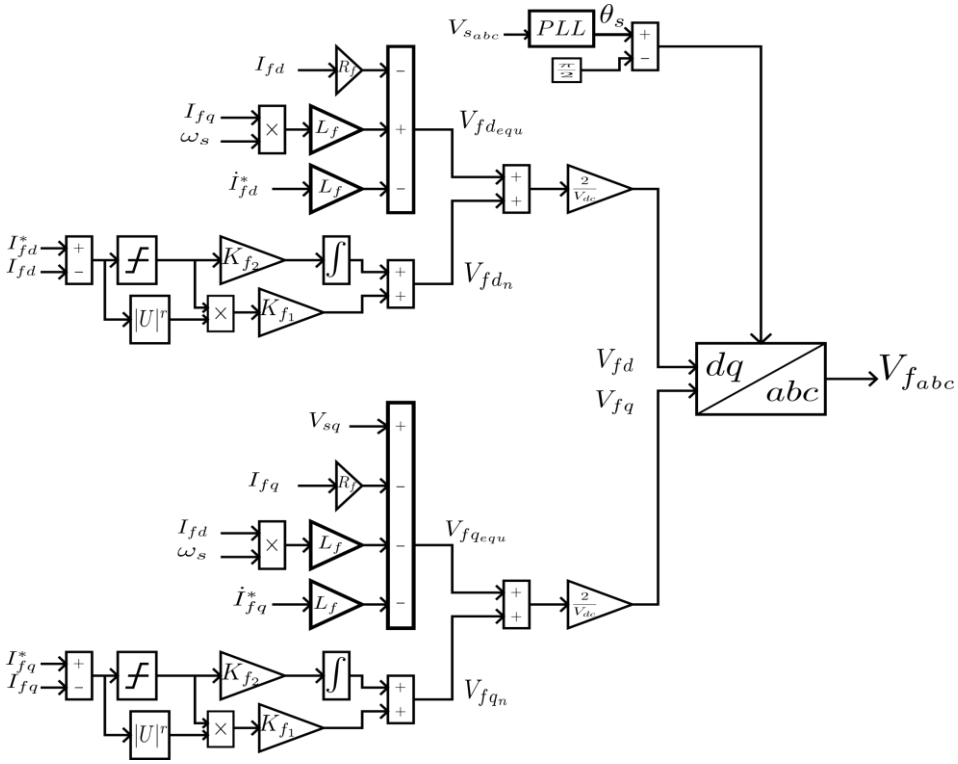

Fig. 8. Diagram of the filter current control.

3. Simulation results

To test the performance of the system, the simulation is performed using MATLAB SimPower System. The system parameters are listed in the appendix (tables 3, 4). Unlike other generators, the DFIG stator cannot be connected to the grid until the synchronization process is verified [21]. In this paper, the DFIG enter to the normal operation after time t = 0.6 s. Fig. 9 shows the profile of the wind speed.

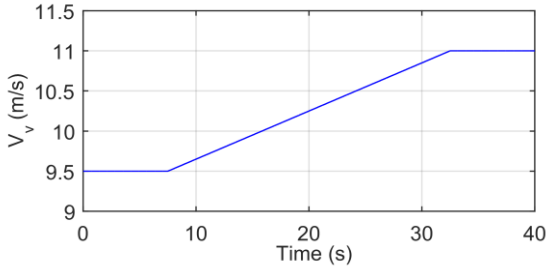

Fig. 9. Profile of the wind speed.

To extract the maximum power from the wind turbine, we have to use the MPPT control to track the optimal speed. Fig. 10 illustrates both the optimal speed and the generator speed.

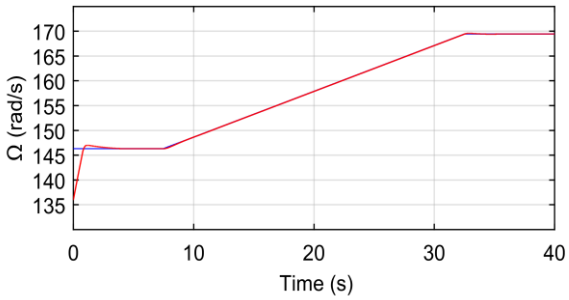

Fig. 10. Optimal and measured generator speed.

In this study, the initial speed is set Ω_{int} = 135 rad/s. It is obvious that the generator speed track very well the desired value. Fig. 11 shows the credibility of MPPT control, where the C_p is around the maximum (C_p = 0.44), although the wind speed is variable.

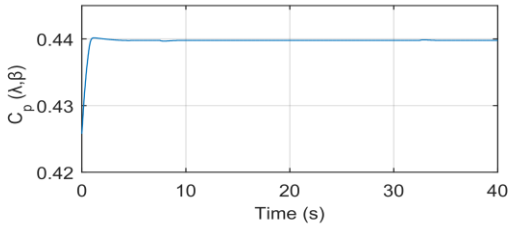

Fig. 11. Power coefficient under variable wind speed.

The reference of the DC bus voltage of the NSC is fixed at 2400 V. In practical work, a charging circuit is used to rise up the DC voltage to a certain value [22]. The aim of this circuit is to protect the system from the inrush current. In this study, this charging circuit was not used but an initial DC bus voltage value is considered when starting the simulation ($V_{dc_{int}}$ = 2200 V in our case). Fig. 12

shows the DC bus voltage. It is obvious the absence of the overshoot and the chattering is very small, which is an advantage for the STC. Fig. 13 presents the active and the reactive power produced by the stator of the DFIG. The reactive power Q_s is set to zero.

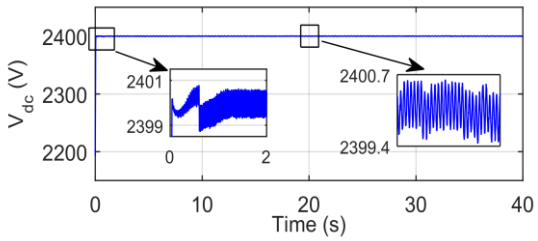

Fig. 12. DC bus voltage.

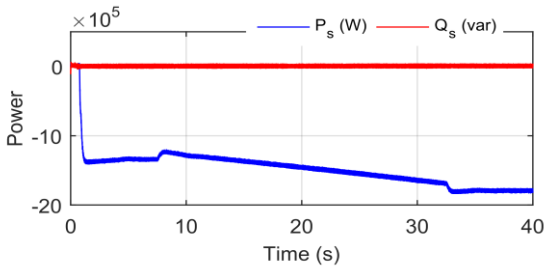

Fig. 13. Active and reactive power of the DFIG stator.

In this paper, a non-linear load is connected to the system which introduces undesirable harmonic currents (see Fig. 1). Two tests have performed to prove the quality of the current produced. Fig. 14 shows the grid current without and with filtering ability in the sub-synchronous mode. The same test is done but in the super-synchronous mode as is illustrated in Fig. 15. It is clear that the NSC has the ability to eliminate harmonics current and to compensate for the reactive power. The current curve is more sinusoidal and the total harmonic distortion (THD) has reduced in both tests. The robustness of the STC was tested and compared with other controllers (SMC and PI). We added ±30% to the initial value of the system parameters ($1.3R_s$; $0.7L_s$; $1.3R_r$; $0.7L_r$; $1.3R_f$; $0.7L_f$; 1.3C and 1.3J). In this paper, we have used a random method to choose the regulator parameters respecting the convergence laws. There are other methods to calculate these parameters by using artificial intelligence to get the optimal choice and it can give us a better result, but they are more complicated.

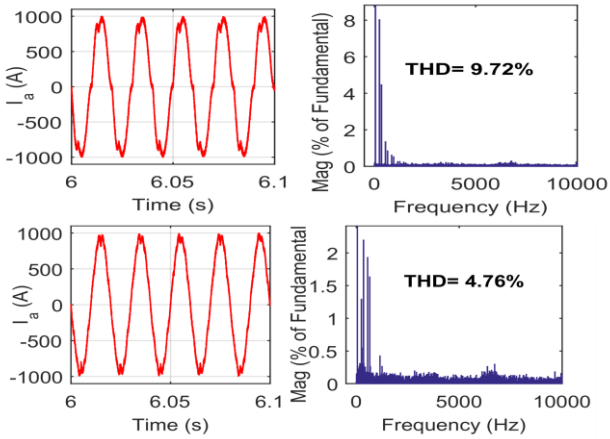

Fig. 14. Grid current analysis in sub-synchronous mode without and with filtering.

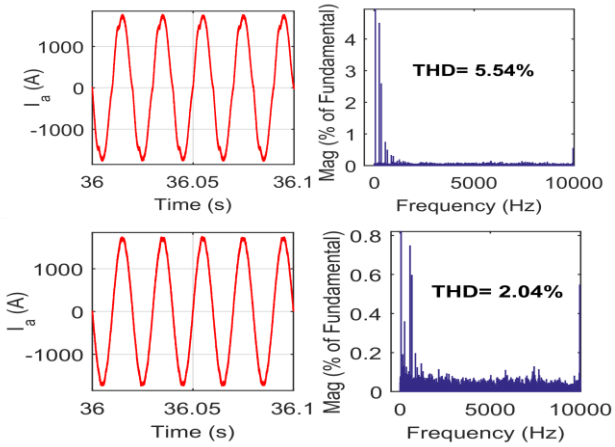

Fig. 15. Grid current analysis in super-synchronous mode without and with filtering.

In Fig. 16, the generator speed is illustrated, and we see that the STC and SMC have high robustness in tracking term unlike the PI controller, which track the reference with a considerable error. The influence of the tracking error can be clearly shown in Fig. 17, where the C_p of the PI controller has decreased, which means the goal of the MPPT is not achieved. Fig. 18 and 19 shows the active and the reactive power produced by the stator. Obviously, the chattering resulting from the SMC is more important than that from the other controllers. Fig. 20 shows the electromagnetic torque of the different regulators. Obviously, the SMC has a high ripple which has a bad influence on the mechanical part. Fig. 21 illustrates the comparison of the DC bus voltage. At the beginning, the PI controller has an overshoot, but it is less than 10% which is a satisfactory result. At time t = 15 s, the zoom shows the high chattering of the SMC compared with the STC and the PI regulators. At time t = 34 s, it is evident that the response of

the PI controller has deviated from the reference value. From the results, it is noticed that the STC has a robust response as the SMC and less chattering as the PI.

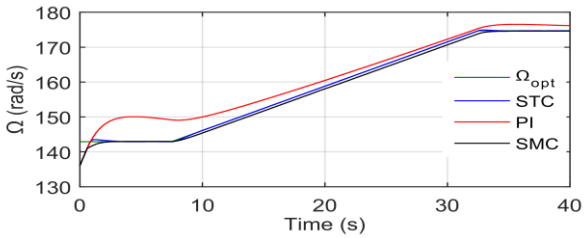

Fig. 16. Comparison of the generator speed of different regulators.

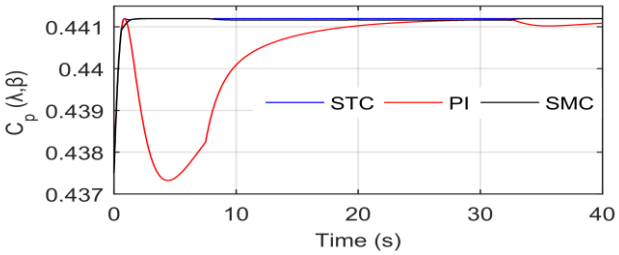

Fig. 17. Comparison of the power coefficient of different regulators.

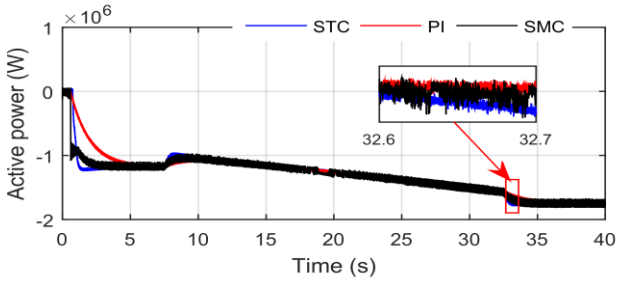

Fig. 18. Comparison of the active power of different regulators.

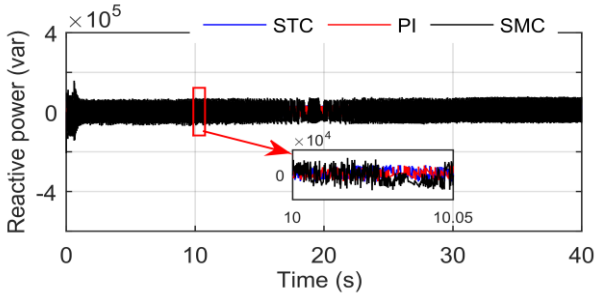

Fig. 19. Comparison of the reactive power of different regulators.

The THD analysis of three regulators is illustrated in table 2. In sub-synchronous mode the THD of the PI is the best where in super-synchronous mode both STC

and PI have a good THD. It is clear that The STC has a satisfactory result compared with SMC.

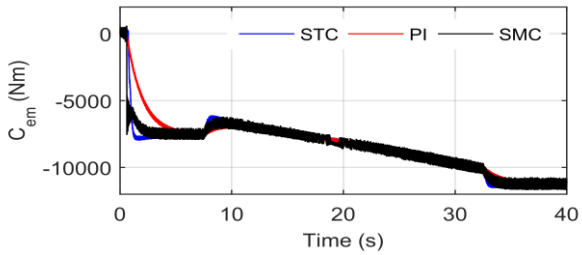

Fig. 20. Comparison of electromagnetic torque of different regulators.

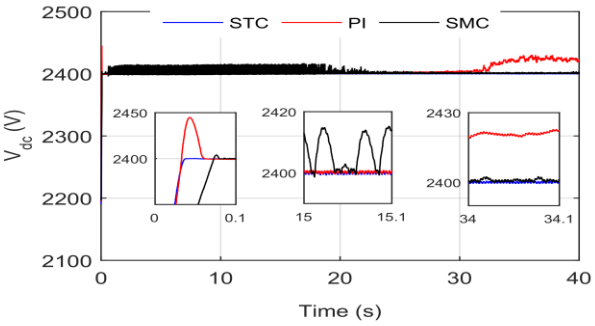

Fig. 21. Comparison of the DC bus voltage of different regulators.

Table 2

Comparison of the THD analysis between the different regulators.

		STC	PI	SMC
THD %	Sub-synchronous	7.16	4.33	23.73
	super-synchronous	2.46	2.28	3.27

4. Conclusions

In this paper, the doubly fed induction generator-based wind turbine is studied, and the simulation is performed using MATLAB SimPower system. The NSC is used to feed the DFIG, and it is controlled with the STC. The system has the ability to eliminate the harmonic currents and to compensate for the reactive power. The robustness of the system is tested by adding ±30% to the nominal system parameters. A comparison between the STC, the SMC and the PI is done to show the effectiveness of the STC. The results show that the STC has the fast convergence and ensure the stability of the system. The chattering is reduced and that ameliorates the quality of the energy and reduces power loss of the NSC. The ripple of the electromechanical torque is reduced which increases the lifetime of the mechanical part. The results of the THD analysis are very satisfactory and they prove the efficiency of the NSC in eliminating harmonic currents. The STC

is a non-linear controller which combine between high robustness and good power quality.

5. Appendix

Table 3

Wind turbine parameters.

Parameter	Value	Unit
P_s	2.0	MW
R_s	2.6	mΩ
R_r	2.9	mΩ
L_s	2.587	mH
L_r	2.587	mH
M	2.5	mH
L_f	1	mH
R_f	0.1	Ω
C	0.38	mF
J	729	Kg. m^2

Table 4

Parameters of the STC

K_{cem_1}	K_{cem_2}	K_{r_1}	K_{r_2}	K_{dc_1}	K_{dc_2}	K_{f_1}	K_{f_2}
5000	7000	50	10	300	50	400	400

R E F E R E N C E S

[1] *F. M. Guangul and G. T. Chala*, SWOT analysis of wind energy as a promising conventional fuels substitute, In 2019 4th MEC International Conference on Big Data and Smart City (ICBDSC), 2019, 1-6 (DOI 10.1109/ICBDSC.2019.8645604).

[2] *REN21*, Renewables 2020 global status report, http://www.ren21.net (accessed 16 October 2020).

[3] *H. T. Jadhav and R. Roy*, A comprehensive review on the grid integration of doubly fed induction generator, International Journal of Electrical Power & Energy Systems, **49**(2013), 8-18 (DOI 10.1016/j.ijepes.2012.11.020).

[4] *K. Ma*, Power electronics for the next generation wind turbine system, Springer, **5**(2015).

[5] *M. Q. Duong, A. Dolara, F. Grimaccia, S. Leva, M. Mussetta and G. Sava*, Fault ride through capability and damping improvement In DFIG, University Politehnica of Bucharest Scientific Bulletin series C-Electrical Engineering and Computer Science, **78**(2016), No. 3, 241-252.

[6] *Y. Dris, M. C. Benhabib and S. M. Meliani*, Selective Control Approach for DFIG Powered by Parallel Inverters, In International Conference in Artificial Intelligence in Renewable Energetic Systems Springer, **102**(2019), 684-692 (DOI 10.1007/978-3-030-37207-1 74).

[7] *B. Belabbas, M. Denai, and T. Allaoui*, A hierarchical control scheme to improve the stability and energy quality of a hybrid wind/photovoltaic system connected to the electricity grid, University Politehnica of Bucharest Scientific Bulletin series C-Electrical Engineering and Computer Science, **82**(2020), No. 2, 307-323.

[8] *M. Shahbazi P. Poure S. Saadate and M. R. Zolghadri*, Five-leg converter topology for wind energy conversion system with doubly fed induction generator, Renewable Energy, **36**(2011), No. 11, 3187-3194 (DOI 10.1016/j.renene.2011.03.014).

[9] *L. Zhang, P. C. Loh and F. Gao*, An Integrated Nine-Switch Power Conditioner for Power Quality Enhancement and Voltage Sag Mitigation, IEEE Transactions on Power Electronics, **27**(2012), No. 3, 1177-1190 (DOI 10.1109/TPEL.2011.2115256).

[10] *N. P. Soe D. M. Vilathgamuwa and K. S. Low*, Doubly fed induction generator for wind energy generation using nine-switch power converter, In IECON 2011-37th annual conference of the IEEE industrial electronics society, (2011), 3608-3613 (DOI 10.1109/IECON.2011.6119895).

[11] *M. Heydari, A. Yazdian Varjani, M. Mohamadian and H. Zahedi*, A novel variable-speed wind energy system using permanent-magnet synchronous generator and nine-switch AC/AC converter, In 2nd Power Electronics drive Systems and Technologies Conference, (2011), 5-9 (DOI 10.1109/PEDSTC.2011.5742490).

[12] *Y. Pang, J. Zhang, D. Xu, C. Yin, Z. Wu, H. Sun, and L. Pan*, Model predictive control of nine switch converter with output filter for independent control of two loads, Journal of Power Electronics, (2020), (DOI 10.1007/s43236-020-00145-0).

[13] *S. Sharma, M. Aware and A. Bhowate*, Direct torque control of symmetrical six-phase induction machine using nine switch inverter, In 2017 IEEE Transportation Electrification Conference (ITEC-India), (2017), 1-6 (DOI 10.1109/ITEC-India.2017.8356952).

[14] *Y. Chen, G. Wen and Y. Kang*, Sliding Mode Pulse Width Modulation (SMPWM) for nine-switch converter, In 2013 IEEE International Symposium on Industrial Electronics, (2013), 1-6 (DOI 10.1109/ISIE.2013.6563653).

[15] *C. Liu, B. Wu, N. R. Zargari, D. Xu and J. Wang*, A novel three-phase three-leg ac/ac converter using nine IGBTs, IEEE Transactions on Power Electronics, **24**(2009), No. 5, 1151-1160 (DOI 10.1109/TPEL.2008.2004038).

[16] *M. E. Azzaoui, H. Mahmoudi, K. Boudaraia and C. Ed-dahmani*, FPGA implementation of super twisting sliding mode control of the doubly fed induction generator, 2017 14th International Multi-Conference on Systems, Signals & Devices (SSD), (2017), 649-654 (DOI 10.1109/SSD.2017.8167021).

[17] *S. Ouchen, M. Benbouzid, F. Blaabjerg, A. Betka and H. Steinhart*, Direct Power Control of Shunt Active Power Filter using Space Vector Modulation based on Super Twisting Sliding Mode Control, In IEEE Journal of Emerging and Selected Topics in Power Electronics, (accepted for publication 2020), 1-12 (DOI 10.1109/JESTPE.2020.3007900).

[18] *A. Ammar, A. Benakcha and A. Bourek*, Closed loop torque SVM-DTC based on robust super twisting speed controller for induction motor drive with efficiency optimization, International journal of hydrogen energy, **42**(2017), No. 28, 17940-17952 (DOI 10.1016/j.ijhydene.2017.04.034).

[19] *A. Gaillard*, Système éolien basé sur une MADA : contribution à l'étude de la qualité de l'énergie électrique et de la continuité de service, PhD Thesis, University of Nancy-I, France, (2010).

[20] *M.C. Benhabib*, A contribution l'étude des différentes topologies et commandes des filtres actifs parallèles structure tension : Modélisation, simulation et validation expérimentale de la commande, Unpublished PhD thesis, Henri Poincare University, France, (2004).

[21] *A. G. Abo-Khalil*, Synchronization of DFIG output voltage to utility grid in wind power system, Renewable Energy, **44**(2012), 193-198 (DOI 10.1016/j.renene.2012.01.009).

[22] *D. Xu, F. Blaabjerg, W. Chen and N. Zhu*, Advanced Control of Doubly Fed Induction Generator for Wind Power Systems, John Wiley & Sons. Chapter 14, (2018), 416-448.